Theor Chem Acc (2012) 131:1218
DOI 10.1007/s00214-012-1218-7

REGULAR ARTICLE

DFT/TDDFT investigation of the stepwise deprotonation in tetracycline: pK_a assignment and UV–vis spectroscopy

Anna Amat · Simona Fantacci · Filippo De Angelis · Benedetta Carlotti · Fausto Elisei

Received: 24 January 2012 / Accepted: 4 April 2012 / Published online: 26 April 2012

Abstract Tetracyclines are a class of derivatives of polycyclic naphthacene carboxamide, which have attracted wide interest in the pharmaceutical field for their use as antibiotics. These molecules are characterized by a substantial conformational flexibility and by the presence of different binding sites which endow tetracycline with a noticeable capability in binding biological targets. A salient property of tetracyclines is the presence of multiple acidic groups: four equilibrium constants have been measured for the fully protonated tetracycline (TCH_3^+) but so far no clear information concerning the pK_as of the various sites has been reported. We present here a computational investigation on the correlation between the acid–base and the spectroscopic properties of this important class of compounds. Starting from the TCH_3^+ species, the pK_a of all the possible deprotonation sites has been computed by DFT calculations. The computed pK_as nicely compare with the experimental data, within 1 pK_a unit, allowing us to individuate the products of the first deprotonation. This procedure has been iteratively repeated using as starting species the products singled out from the previous deprotonation, thus individuating the stepwise products of each deprotonation step. Then, the optical absorption spectra have been computed for all the species involved in the protonation/deprotonation equilibria, comparing the results with the experimental data. The good agreement between theory and experiment has allowed us to rationalize the correlation between the solution pH and the absorption spectra.

Keywords Theoretical pK_a assignment · DFT/TDDFT calculations · Simulation of UV–vis spectra

1 Introduction

Tetracyclines are a family of derivatives of polycyclic naphthacene carboxamide that have attracted wide interest due to their pharmaceutical properties [1–7], mainly related to their broad-spectrum antibiotic activity [8, 9]. Besides this widely recognized application, they have also been used in the field of gene regulation and as inhibitors of the metalloproteinase activity [10, 11]. Due to tetracycline's various applications, the number of publications on this topic has quickly grown in the last years [1–25]. The conformation flexibility and the presence of different complexation sites are among the reasons of tetracycline's success in binding biological targets [12]. Tetracyclines posses various carbonyl and hydroxyl groups which open the way to different complexation modes with metal ions [12]. Despite their clear role in pharmacology, tetracyclines have shown some side effects due to their phototoxicity and photosensitizing action [1, 26–28]. Moreover, it is well known that the pharmaceutical activity of these compounds is strongly dependent on the environment, both in terms of

Electronic supplementary material The online version of this article (doi:10.1007/s00214-012-1218-7) contains supplementary material, which is available to authorized users.

A. Amat (✉) · S. Fantacci (✉) · F. De Angelis
Istituto CNR di Scienze e Tecnologie Molecolari (ISTM), c/o Dipartimento di Chimica, Università di Perugia, Via elce di Sotto 8, 06213 Perugia, Italy
e-mail: anna@thch.unipg.it

S. Fantacci
e-mail: simona@thch.unipg.it

B. Carlotti · F. Elisei
Dipartimento di Chimica and Centro di Eccellenza sui Materiali Innovativi Nanostrutturati (CEMIN), Università di Perugia, Via elce di Sotto 8, 06213 Perugia, Italy

solvent and pH [1, 47]. Therefore, the comprehension of tetracyclines acid–base chemistry and its influence on their spectroscopic properties is crucial to study the damaging effects of light irradiation and to further tailor their pharmaceutical use.

The fully protonated tetracycline (TCH_3^+) presents four possible deprotonation sites in positions 3, 4, 10, and 12, see Scheme 1. Four equilibrium constants associated to mono-deprotonation reactions have been measured at 3.4, 7.3, 9.0, and 11.8. These pK_a values lead from the fully protonated (TCH_3^+) to the zwitterionic (TCH_2), the mono-anionic (TCH^-), and finally to the di-anionic (TC^{2-}) forms [1, 43–46].

Several theoretical investigations on tetracyclines have been reported, using ab initio [29–32] and DFT [33–40] calculations, dealing with their possible conformations [35–37], their complexation with different metals [33, 39, 40], and their vibrational and NMR spectroscopy [34, 35]. Regarding the electronic spectra, the simulation of the absorption spectra has been performed for the neutral tetracycline [2] and for the related anhydrotetracycline by semiempirical calculations [41]. In a recent study, the relative stabilities of several tetracycline conformations in the excited state have been investigated using TDDFT to evaluate the pathways of excited-state intra-molecular proton transfer [11]. Although the pK_as of tetracycline have been largely studied experimentally, to the best of our knowledge they have never been computed using first principle methods nor the absorption features of all the possible protonated/deprotonated forms have been computed. To our knowledge, only two computational studies have provided an estimation of tetracycline pK_a; the first one employs the SPARC calculator, based on a database of broad range of organic compounds families pK_as [46], while the second one combines semiempirical calculations with fitting of experimental data [42].

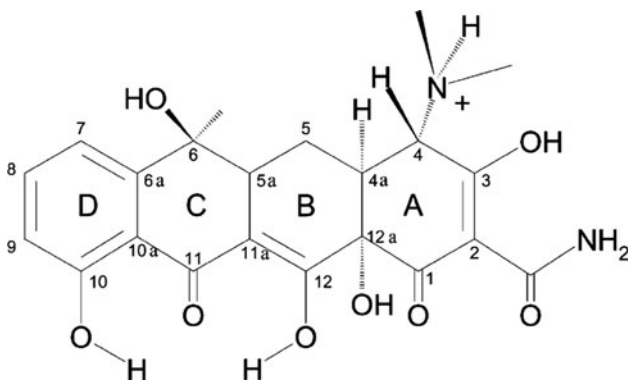

Scheme 1 Chemical structure of fully protonated tetracycline (TCH_3^+) and sites numbering

In this work, we present an integrated theoretical and experimental study on the acid–base properties of tetracycline and on their influence on its electronic absorption spectra. Starting from the fully protonated species (TCH_3^+), we have computed the pK_a of the four possible deprotonation sites. The investigated neutral species, obtained by deprotonation of TCH_3^+, have been labeled $TCH_2(m)$, where the m index refers to the deprotonation site, with reference to the labels defined in Scheme 1. With the pK_a calculations, the product from the first deprotonation has been individuated and the procedure has been iteratively repeated thus assigning the species produced at each equilibrium stage. The products obtained from the second and third deprotonation have been labeled $TCH^-(m, n)$ and $TC^{2-}(m, n, j)$, respectively, where m, n, and j indexes refer to the first, second, and third deprotonation site, respectively. The absorption spectra of the individuated products of each deprotonation step have been simulated and compared to the experimental spectra at intermediate pHs. TDDFT has become a powerful tool to understand and even predict the electronic optical properties of many species with accuracies usually within 0.20 eV [48–50] for the neutral species. The description of the spectroscopic properties of negatively charged species is often more challenging. In these cases, a hybrid continuum polarizable model with the inclusion of explicit solvent molecules might consistently improve the accuracy [48].

In this investigation, the computed spectra have been used to assign the main absorption bands, analyzing the involved electronic transitions, and the changes on the electronic properties going from the protonated to the corresponding deprotonated species have been rationalized.

Our calculations point out that the stepwise deprotonation of TCH_3^+ takes place in the hydroxyl 3, hydroxyl 12, ammonium 4, and hydroxyl 10 groups, respectively. Regarding the effects of pH on the absorption spectra, the obtained results show that for the zwitterionic (first deprotonation), the mono-anionic (second deprotonation), and the di-anionic forms (third deprotonation) the first band is mainly due to π–π^* transitions involving the BCD chromophore, Scheme 1, while for the fully protonated TCH_3^+ the first band is originated essentially by charge-transfer transitions having as final states orbitals delocalized also on the A ring. On overall, our calculated UV–vis spectra are in fair agreement with the experimental data, further supporting the proposed pK_a assignment.

2 Computational methodology

All the calculations have been performed by means of DFT [51] and its time-dependent version (TDDFT) [52–54] as

implemented in the Gaussian09 (G09) program package [55], using the B3LYP [56–58] hybrid functional and the 6-31+G^* [59, 60] basis set. Calculations in water solution have been carried out by means of the Conductor-like Polarizable Continuum Model (CPCM) [61]. Geometry optimizations with no symmetry constraints have been performed on all the investigated systems both in vacuo and in solution.

The absolute pK_as have been computed combining the results in gas phase and in solution. Among the various reported approaches which provide fairly good results in calculating the pK_as [62–69], we have followed the procedure detailed in Ref. [68, 69]. Accordingly, the pK_a has been computed as:

$$pK_a = \left(G_{gas}(A^-) + G_{gas}(H^+) - G_{gas}(AH) + \Delta G_{sol}(A^-) + \Delta G_{sol}(H^+) - \Delta G_{sol}(AH)\right)/2.303RT \quad (1)$$

where $G_{gas}(A^-/AH)$ is the Gibbs energy in gas phase for the deprotonated/protonated species and $\Delta G_{sol}(A^-/AH)$ is the difference between $G_{sol}(A^-/AH)$, the Gibbs energy in solution of the deprotonated/protonated species, and $G_{gas}(A^-/AH)$. G_{gas} has been computed on the geometries optimized in gas phase, taking into account the thermal corrections by performing frequency calculations on the optimized structures, while ΔG_{sol} has been computed on the molecular structures optimized in solution together with a reference calculation in vacuo.

The pK_a calculation is based on the absolute solution free energy of the proton, which cannot be really measured directly in experiment, indeed becoming a complicated issue widely discussed in literature.

For $G_{gas}(H^+)$ we employed the value −6.28 kcal/mol, as obtained from the Sackur–Tetrode equation [70]. $G_{gas}(H^+)$ uses a reference state of 1 atm; therefore, the value of $G_{gas}(H^+)$ has been state corrected using [68, 71]:

$$\Delta G^{(1atm \rightarrow 1mol)} = RT \ln(24.46)$$

Different values have been successfully used in literature for $\Delta G_{sol}(H^+)$, as the ones proposed by Liptak (−264.61) [69], Zhan and Dixon [72, 73] (−264.3 kcal/mol), or Tissandier [74] (−264.0 kcal/mol). These values differ by only 0.3 and 0.6 kcal/mol, which in the calculation of pK translates into a rigid shift smaller than 0.5 pK_a units. In principle, this would have no influence on the relative acidities of the different species discussed in this work and is, however, below the accuracy of the employed methodology [71, 75]. Following our previous investigations [48, 62, 63], we have chosen to use the −264.61 kcal/mol value for $\Delta G_{sol}(H^+)$ (69). Therefore for all the pK_a calculations, in the Eq. (1) we use as absolute value of $G_{sol}(H^+)$ −269.0 kcal/mol, which accounts for $G_{gas}(H^+) = -6.28$ kcal/mol, $\Delta G_{sol}(H^+) = -264.61$ kcal/mol, and $\Delta G_{sol}^{(1atm \rightarrow 1mol)} = 1.9$ kcal/mol at T = 298K.

The procedure used for the pK_a calculations usually leads to deviations with the experiment, which are within 1–2 pK_a units [71, 75]. However, for negatively charged species, the description of the solvation energy using only a continuum model can introduce larger errors [76]. For these species, the solvation energy calculations could be improved with a combination of a continuum and an explicit solvation model [75, 77].

The comparison between the microscopic pK_as computed for the single species and the macroscopic experimental ones is a simplification. The presence of different species could be accounted for by computing the tautomerization constants of the different species and their concentration ratios [78, 79]. Given the complexity of the studied system, too many species should be considered and this would largely complicate the investigated scenario. Therefore, this procedure is hardly feasible here due to tetracycline size and conformation flexibility.

The 60 lowest TDDFT singlet–singlet transitions have been computed in water solution at the ground-state optimized geometries using the same level of calculation. The computed transitions have been convoluted with gaussian functions with a σ value of 0.2 eV to simulate the absorption spectra. For clearness, the intensity of the experimental absorption spectra has been scaled to match that of the lowest energy computed absorption bands.

Since it has been reported that B3LYP exchange–correlation (xc) functionals might fail in the description of charge-transfer states [80, 81], we have checked the TDDFT calculations with two other xc functionals, namely M06 [82] and PBE0 [83, 84]. Results obtained show that, while using the two latter xc functionals we have a better agreement with the experiment for the TCH_3^+ regarding the relative intensities of the computed bands, for the negatively charged species M06 and PBE0 computed spectra show larger discrepancies with the experiment in terms of energy than B3LYP. On overall, the three xc functionals do not present very large differences showing a fair agreement with the experiment. Since the pK_a calculations have been performed with B3LYP, the theoretical spectra reported here are computed using the same level of calculation, while the simulated spectra computed with M06 and PBE0 xc functionals are reported in the Supporting Information (SI).

3 Experimental methodology

Absorption spectra were recorded with a Perkin-Elmer Lambda 800 spectrophotometer. Tetracycline was a Sigma-Aldrich product and used without further purification. The pH of aqueous solutions was adjusted by Britton buffers in the 2–12 pH range.

4 Results and discussion

4.1 The fully protonated TCH_3^+ system

Two different geometrical tautomers corresponding to a twisted and an extended conformation have been optimized for the fully protonated TCH_3^+. The extended conformation has been computed 5 kcal/mol more stable than the twisted one in solution, in line with previous stability data [42]. The optimized geometry of the extended conformation of TCH_3^+ is reported in Fig. 1a together with the optimized molecular structures of all the possible products of the stepwise deprotonations (Fig. 1, panels b–d) that will be discussed in the next sections.

The absorption spectrum has been computed and compared to experimental data, assigning the main transitions. The results are reported in Fig. 2 together with the energy and selected isodensity plots of the frontier molecular orbitals. The wavelength, energy, oscillator strength, and character in terms of involved molecular orbitals of the main electronic transitions originating the absorption bands have been reported in Table 1.

The experimental UV–Vis absorption spectrum at pH = 2.4 shows two UV absorption bands at ca. 358 nm and 270 nm. The low-energy band has a steep decrease toward the low-energy region while a broader tail is retrieved between 350 and 300 nm. The computed spectrum is in good agreement with the experimental one, even though a slightly different intensity distribution is calculated, which provides a different band shape compared to the experimental data. The lowest energy band is composed by three transitions of similar intensity that correspond to $S_0 \rightarrow S_1$, $S_0 \rightarrow S_3$, and $S_0 \rightarrow S_4$ excitations. $S_0 \rightarrow S_1$ is responsible for the peak at 358 nm and corresponds manly to the HOMO $\rightarrow$ LUMO transition. The HOMO of TCH_3^+ has a π character and is mainly localized in the D ring (Fig. 2) with contributions coming from the hydroxyl oxygen atoms, while the LUMO is essentially delocalized

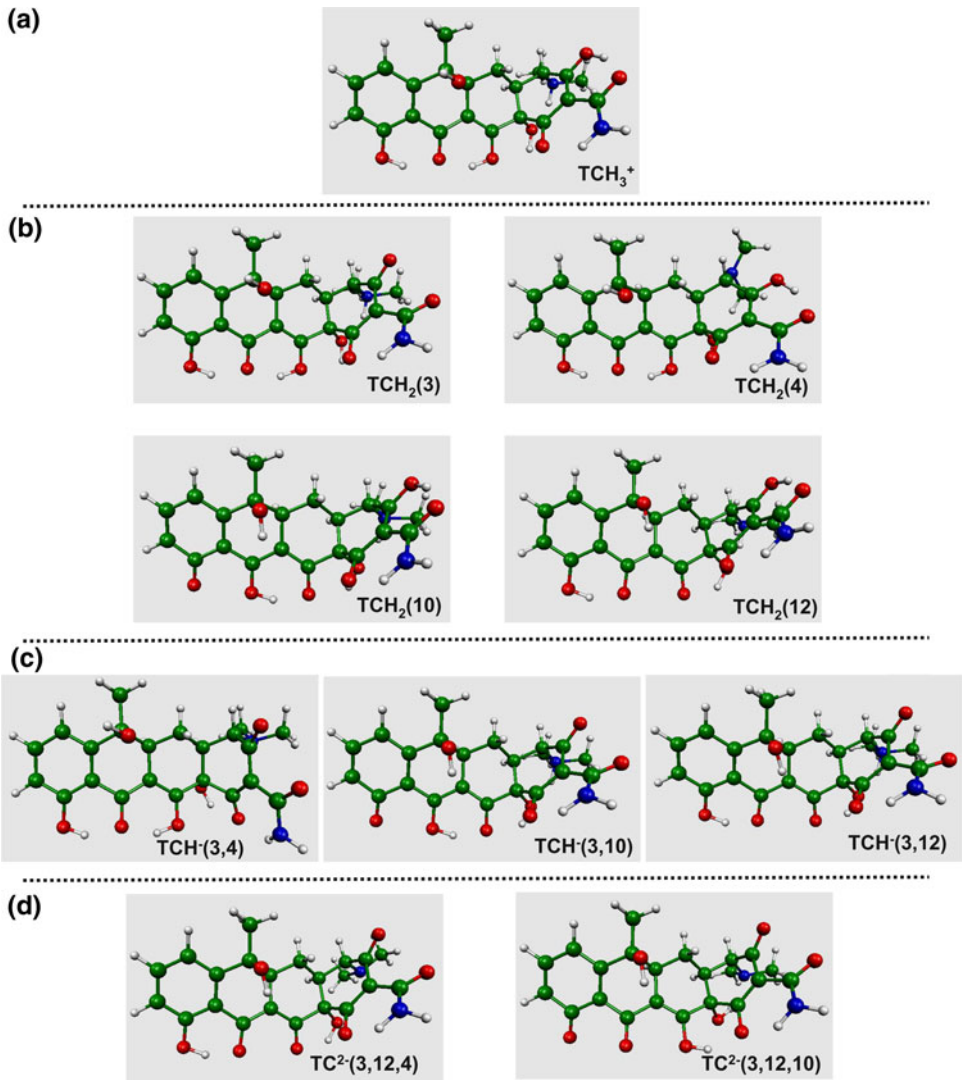

Fig. 1 Optimized structures in water of all the investigated species. **a** fully protonated TCH_3^+, **b** first deprotonation $TCH_2(n)$, **c** second deprotonation $TCH^-(3,n)$, and **d** third deprotonation $TC^{2-}(3,12,n)$

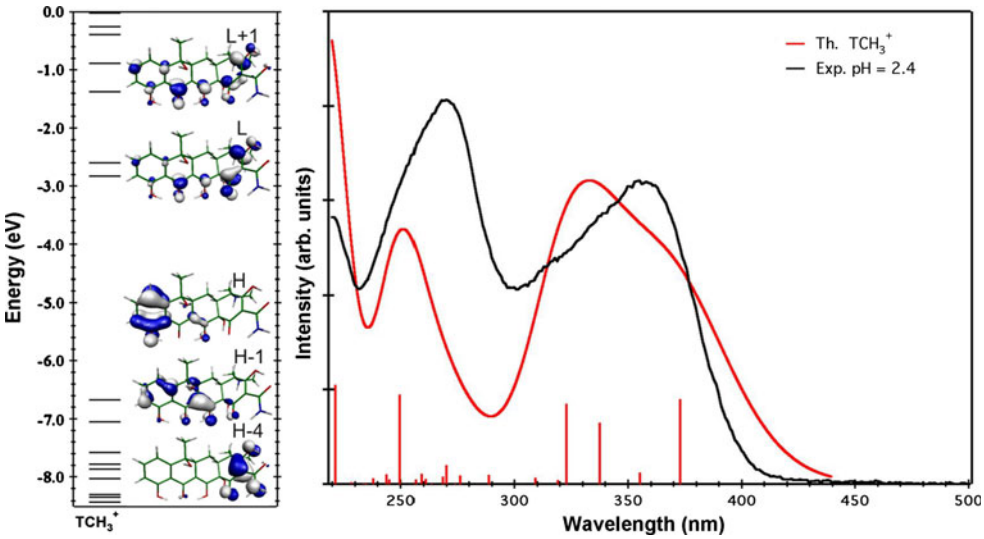

Fig. 2 *Left*: TCH_3^+ molecular orbital energies and isodensity plots. *Right*: Experimental spectrum measured at pH = 2.4 (*black*) versus computed spectrum of TCH_3^+ (*red*)

Table 1 Experimental (pH = 2.4) and calculated absorption maxima of TCH_3^+, transition wavelengths and energies, oscillator strengths, and composition in terms of molecular orbitals

Exp. max. (nm/eV)	Th. max. (nm/eV)	Th. trans. (nm/eV)	*f*	Composition
358/3.47	354/3.50	373/3.32 (S_1)	0.1751	H → L (86 %)
		338/3.67 (S_3)	0.1312	H → L+1 (50 %)
				H-1 → L (32 %)
		323/3.84 (S_4)	0.1740	H-1 → L+1 (62 %)
270/4.59	250/4.96	250/4.96 (S_{16})	0.1946	H-4 → L+1 (58 %)
				H-4 → L (16 %)
				H-7 → L (13 %)

throughout the phenolic and carbonyl carbons and their corresponding oxygen atoms, with a higher percentage in position 3 of ring A. The $S_0 \rightarrow S_3$ and $S_0 \rightarrow S_4$ transitions can be considered responsible for the broadening of the band in the 350–300 nm region. Both transitions involve the HOMO and HOMO-1 as starting states, with the HOMO-1 delocalized in the BCD rings, while the arriving states are the LUMO and LUMO+1, which show a similar electronic delocalization. The experimental lowest energy band has therefore a dominant charge-transfer (CT) character. The band at 270 nm is manly originated by an intense transition with a π–π^* character from the HOMO-4 and HOMO-7, both orbitals localized in the A ring, to the LUMO and LUMO+1.

4.2 First deprotonation

The TCH_3^+ species shows four deprotonation sites labeled as 3, 4, 10, and 12 in Scheme 1. We have taken into consideration all the possible deprotonation products, computing their respective pK_as. The hydroxyls bound to sp^3 carbons, OH(6) and OH(12a), were not taken into account for deprotonation, due to their expected high pK_a. Out of the four possible mono-deprotonated species, we find three zwitterionic species, TCH_2(3), TCH_2(10), and TCH_2(12) and a neutral one, TCH_2(4), see Fig. 1b. No significant changes are retrieved in the optimized molecular structures of these species compared to that of TCH_3^+. The calculated G_{gas}, ΔG_{sol}, and pK_a values species are reported in Table 2.

The most acidic site is computed to be site 3, with a pK_a of 2.5 to be compared to the experimental pK_a of 3.4. The computed pK_a, which differs from the experimental reference value by less than one pK unit, can be considered within the accuracy of the employed methodology. Further pK_as are computed at 3.9 and 4.1 for TCH_2(4) and TCH_2(12), respectively, which are distant enough from the first pK_a to assign the first deprotonation to site 3. On the other hand, a very high $pK_a = 10.6$ is computed for site 10. Since the theoretical results point out that first deprotonation product is TCH_2(3), its absorption spectrum has been computed and compared to the experimental spectrum at pH = 4.8. The comparison between the experimental and simulated spectra is reported in Fig. 3 and Table 3, together with the frontier molecular orbitals (energy and isodensity plots) of the TCH_2(3) species, Fig. 3.

Table 2 Gibbs free energy in gas phase, solvation ΔG and pK_a computed for the first deprotonation

Site	$G_{gas}(TC^+)$ (hartree)	$\Delta G_{sol}(TC^+)$ (kcal/mol)	$G_{gas}(TC)$ (hartree)	$\Delta G_{sol}(TC)$ (kcal/mol)	pK_a
3	−1,564.139157	−54.42	−1,563.737273	−34.22	2.5
4	−1,564.139157	−54.42	−1,563.767209	−13.45	3.9
10	−1,564.139157	−54.42	−1,563.700700	−46.05	10.6
12	−1,564.139157	−54.42	−1,563.724709	−39.92	4.1

The experimental spectrum at pH = 4.8 has a maximum at 358 nm, which is unaltered with respect to the spectrum registered at a 2.4 pH. However, a plateau is found between 300 and 320 nm, consistent with the presence of medium-to-small intensity transitions in this region. The band at high energies is red-shifted to 275 nm with respect to the spectrum at lower pH, with a shoulder appearing at ca. 250 nm.

All the experimental features of the spectrum at pH = 4.8 and the main differences with respect to the TCH_3^+ case are well reproduced by the TDDFT absorption spectrum of TCH_2(3). The longest wavelength simulated UV band is originated by a single transition, $S_0 \rightarrow S_2$, (Table 3) computed at 363 nm with HOMO-1 → LUMO character. The HOMO-1 of the TCH_2(3) has a π character with a similar electronic distribution to that computed for the HOMO of TCH_3^+. The $S_0 \rightarrow S_5$ and $S_0 \rightarrow S_7$ excitations are responsible for the plateau region of the experimental spectrum. Both transitions show the LUMO as arriving state; the LUMO shows the electronic charge delocalized over the BCD rings with contributions coming from the p orbitals of the oxygen atoms. The LUMO of TCH_2(3) differs from that of the fully protonated species for the absence of charge density in the A ring.

In the higher energy region, the spectral profile of the experimental band is qualitatively reproduced by our TDDFT calculations, even though the computed band maximum is blue-shifted with respect to the experiment. The transition directly related to the band maximum at 262 nm ($S_0 \rightarrow S_{12}$) has a HOMO → LUMO+1 character, with the arriving state located in the A ring with a similar electronic charge distribution computed for TCH_3^+, see Fig. 3, while the shoulder is originated by a series of transitions from the HOMO to arrival states higher than the LUMO+1.

4.3 Second deprotonation

Having established that the first deprotonation takes place in site 3, we considered all the possible deprotonation products derived from the TCH_2(3) species and thus computed the pK_as for the three remaining sites, namely 4, 10, and 12. The 3 possible anionic species arising from these deprotonations have been labeled TCH^-(3,4), TCH^-(3,10), and TCH^-(3,12), respectively. Interestingly, while no significant differences are retrieved for TCH^-(3,4) and TCH^-(3,12) geometries, deprotonation in site 10 leads to an internal proton transfer of the H in position 12 to the ketonic oxygen in site 11. The optimized structures are reported in Fig. 1c while the G_{gas}, ΔG_{sol}, and pK_a computed for each species are reported in Table 4.

The most acidic site is computed to be site 12 with a pK_a of 7.0 in excellent agreement with the experimental pK_a of 7.3. The higher computed values are 8.4 and 13.2 for

Table 3 Experimental (pH = 4.8) and theoretical absorption maxima of TCH_2(3), main computed transition wavelength and energies, oscillator strengths, and composition in terms of molecular orbitals

Exp. max. (nm/eV)	Th. max. (nm/eV)	Th. trans. (nm/eV)	f	Composition
358/3.46	363/3.42	363/3.42 (S_2)	0.3716	H-1 → L (95 %)
313/3.96 (sh)	317/3.91 (sh)	317/3.91 (S_5)	0.1053	H-4 → L (49 %)
				H-8 → L (25 %)
		307/3.91 (S_7)	0.0605	H-8 → L (42 %)
				H-4 → L (37 %)
275/4.51	262/4.73	266/4.66 (S_{12})	0.2232	H → L+1 (86 %)
250/4.96 (sh)	242/5.12 (sh)	255/4.86 (S_{14})	0.0480	H-6 → L (72 %)
		248/5.00 (S_{16})	0.0899	H → L+2 (55 %)
				H → L+3 (24 %)
		240/5.16 (S_{19})	0.1044	H → L+3 (56 %)
				H → L+2 (19 %)

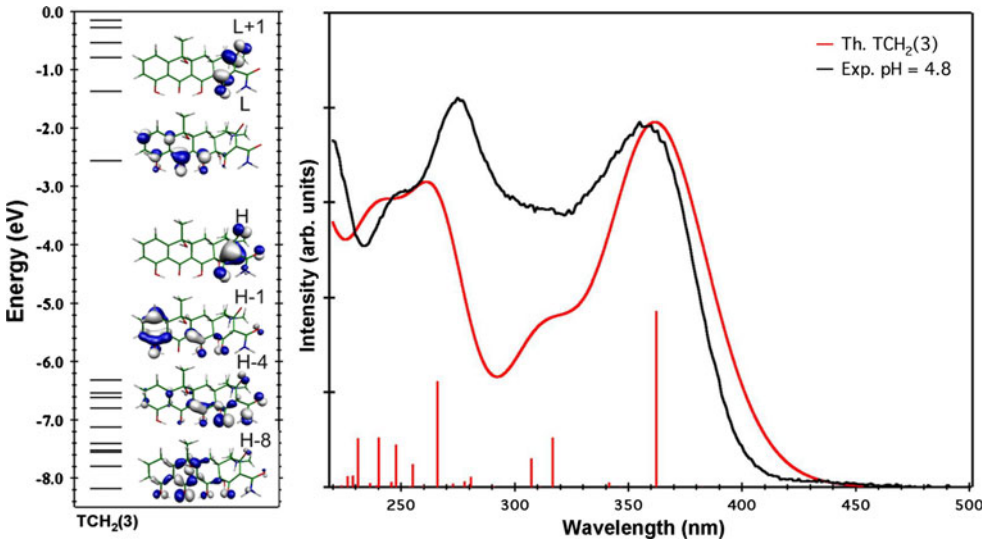

Fig. 3 *Left*: $TCH_2(3)$ molecular orbital energies and isodensity plots. *Right*: Experimental spectrum pH = 4.8 (*black*) versus computed spectrum of $TCH_2(3)$ (*red*)

Table 4 Gibbs free energy in gas phase, solvation ΔG and pK_a computed for the second deprotonation

Site	G_{gas}(TC) (hartree)	ΔG_{sol}(TC) (kcal/mol)	$G_{gas}(TC^-)$ (hartree)	$\Delta G_{sol}(TC^-)$ (kcal/mol)	pK_a
4	−1,563.737273	−34.22	−1,563.249047	−60.10	8.4
10	−1,563.737273	−34.22	−1,563.216577	−74.02	13.2
12	−1,563.737273	−34.22	−1,563.232038	−72.68	7.0

$TCH^-(3,4)$ and $TCH^-(3,10)$, respectively. The computed absorption spectra of the $TCH^-(3,12)$ species compared to the experimental data are reported in Fig. 4 and Table 5.

The experimental spectrum at pH = 8.5 has a single band in the lower energy region measured at 371 nm that is narrower and red-shifted by ca. 0.10 eV with respect to the same band of the spectrum at 4.8 pH. The plateau region observed at pH = 4.8 has disappeared while the spectrum in the high-energy region is almost unchanged with a maxima at 272 nm and a shoulder at 249 nm.

The simulated spectrum of the $TCH^-(3,12)$ species is blue-shifted by ca. 0.15 eV with respect to the experiment. For this species, the difference between theory and experiment is slightly larger than in the former cases, even if it remains within the limit of the methodology accuracy. Since a pK_a of 8.4 was computed for the $TCH^-(3,4)$

Table 5 Experimental (pH = 8.5) and theoretical absorption maxima of $TCH^-(3,12)$, main computed transition wavelength, oscillator strength, and composition in terms of molecular orbitals

Exp. max. (nm/eV)	Th. max. (nm/eV)	Th. trans (nm/eV)	f	Composition
371/3.34	353/3.51	355/3.50 (S_1)	0.2041	H → L (50 %)
				H-2 → L (20 %)
				H-3 → L (19 %)
		351/3.55 (S_2)	0.2019	H → L (47 %)
				H-2 → L (27 %)
				H-3 → L (13 %)
272/4.56	264/4.69	266/4.67 (S_{12})	0.1629	H-1 → L+1 (54 %)
				H-9 → L (12 %)
249/4.98 (sh)	243/5.10 (sh)	246/5.06 (S_{19})	0.1002	H-1 → L+2 (30 %)
				H-1 → L+3 (23 %)
				H-8 → L+1 (12 %)
		243/5.11 (S_{20})	0.0685	H-8 → L+1 (24 %)
				H-1 → L+2 (22 %)

species, close to the 8.5 pH at which the spectrum was measured, we checked the possibility that the blue-shift with respect to the experimental spectrum was due to the presence of this species at the given pH. However, the simulated spectrum of the TCH^-(3,4) species is very similar to that computed for TCH^-(3,12), see Supporting Information, excluding this hypothesis as the origin of the deviation. The presence of a folded conformation at high pH was also investigated by optimizing the TCH^-(3,12) folded species. The optimized folded structure is 9 kcal/mol less stable than the extended one. It can be therefore concluded that neither the presence of the folded TCH^-(3,4) nor the TCH^-(3,12) species can be the cause of the theory/experiment differences. The overestimation of the lowest energy band is probably due to the difficulties arising from the treatment of the specific solute–solvent interactions with a continuum solution model in charged species, as observed for related organic systems [48].

The lowest energy band is formed by two almost isoenergetic transitions with a very similar composition in terms of HOMO → LUMO and HOMO-2 → LUMO, Table 5. The involved starting and the arriving states are delocalized in the BCD chromophore. The HOMO has a mixed π–n character with the charge localized mainly between C11 and C12 and the corresponding carbonyl oxygens (lone pairs), (Fig. 4) where the deprotonation has taken place, contrarily to the HOMO and HOMO-1 of TCH_3^+ and TCH_2(3) where the occupied orbital involved in the transition was localized in ring D. The HOMO-2 and the LUMO are bonding and antibonding π combinations, respectively, delocalized over the whole BCD chromophore. Upon deprotonation in site 12, the lowest π–π^* absorption band shows a partial n–π^* character. In the high-energy region, the band at 272 nm and the shoulder at 249 nm are characterized by a series of transitions to higher unoccupied orbitals. The most intense transition in this region is computed at 264, has a π–π^* character, and is completely located within the A ring.

4.4 Third deprotonation

Considering as reference the species TCH^-(3,12), we have computed the pK_as for the two remaining deprotonation sites, namely 4 and 10. The two possible di-anionic species arising from these deprotonations are labeled TC^{2-}(3,12,4) and TC^{2-}(3,12,10), respectively. Similarly to what retrieved for the second deprotonation, the third deprotonation in site 10 leads to significant changes in the molecular structure. In particular, we find the occurrence of two internal proton transfers: one from H in site 12a to site 12 and another from the dimethylamino group, site 4, to site 12a, see Scheme 1 and Fig. 1d. The optimized structures are reported in Fig. 1d while the G_{gas}, ΔG_{sol}, and pK_a computed for each species are reported in Table 6.

The computed pK_as are 12.6 and 21.4 for the sites 4 and 10, respectively. The lowest computed pK_a is 2.5 units

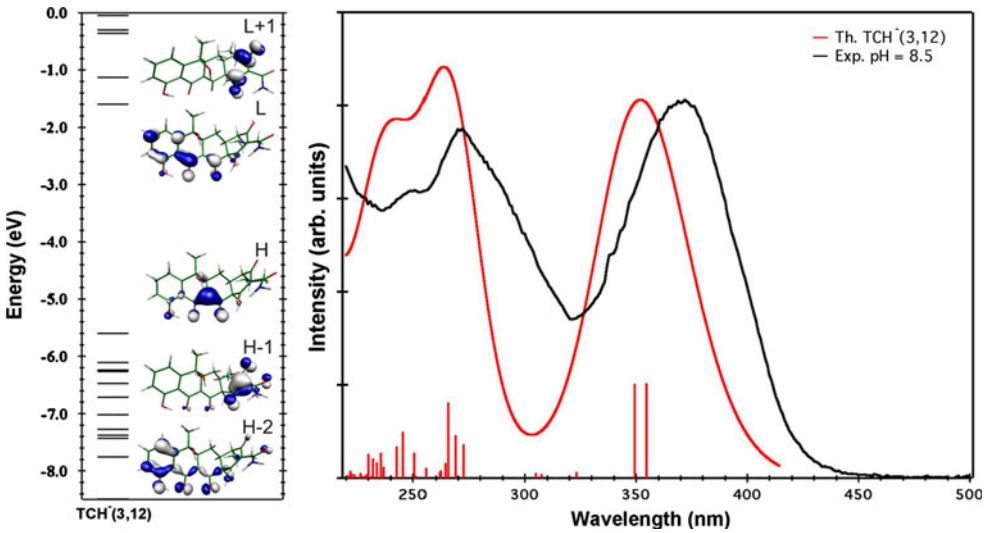

Fig. 4 *Left*: TCH^-(3,12) molecular orbital energies and isodensity plots. *Right*: Experimental spectrum pH = 8.5 (*black*) versus computed spectrum of TCH^-(3,12) (*red*)

Table 6 Gibbs free energy in gas phase, solvation ΔG and pK_a computed for the third deprotonation

Site	$G_{gas}(TC^-)$ (hartree)	$\Delta G_{sol}(TC^-)$ (kcal/mol)	$G_{gas}(TC^{2-})$ (hartree)	$\Delta G_{sol}(TC^{2-})$ (kcal/mol)	pK_a
4	−1,563.232038	−72.68	−1,562.646612	−153.90	12.6
10	−1,563.232038	−72.68	−1,562.623695	−156.25	21.4

higher than the experimental one measured at 9.0. Different solvation methods, that is, SVPE [85], PCM [86], IEFPCM [87], and COSMO [88], were evaluated for a series of amino compounds by Lu et al. [78]. Linear fitting between the experimental and computed pK_as resulted in rmsd values of 1.18 and 3.21 for the SVPE and the PCM method. Though the use of SVPE for the inclusion of the solvent effects could improve the agreement with the experiment, probably the discrepancy computed for the TC^{2-}(3,12,4) species is also due to an overestimated destabilization of the di-anion species with respect to the mono-anionic species, and for the consistency sake, we maintained here the solvation method used for the previous calculations.

In any case, the pK_a of site 4 is consistently lower than that one of site 10, so that the latter deprotonation process can be excluded. We have therefore computed the absorption spectrum for the TC^{2-}(3,12,4) species, which is compared to the experimental one at pH = 9.2 in Fig. 5 and Table 7. On the left of Fig. 5, the energy levels and the isodensity plots of the frontier molecular orbitals are shown.

The experimental spectrum at pH = 9.2 possesses a low-energy band at 376 nm and high-energy band at 270 nm and is very similar to that measured at pH = 8.5, with only the first band slightly red-shifted by ca. 0.05 eV. The computed spectrum of the TC^{2-}(3,12,4) species is again slightly blue-shifted with respect to the experimental spectrum at pH = 9.2, but we still obtain a fairly good agreement. The lowest absorption band is composed by two transitions: the most intense one, computed at 353 nm, has mainly HOMO → LUMO character with the same electronic charge distribution shown by the corresponding transition of TCH^{-}(3,12). The higher energies region shows a series of transitions having as starting states the HOMO, HOMO-1, and HOMO-2 and as arriving states the LUMO/LUMO+2 set.

Table 7 Experimental (pH = 9.2) and theoretical absorption maxima of TC^{2-}(3,12,4), main computed transition wavelengths and energies, oscillator strengths, and composition in terms of molecular orbital

Exp. max. (nm/eV)	Th. max. (nm/eV)	Th. trans (nm/eV)	*f*	Composition
376/3.30	356/3.48	365/3.40 (S_1)	0.1041	H-3 → L (41 %)
				H → L (29 %)
				H-2 → L (10 %)
		353/3.51 (S_2)	0.2895	H → L (67 %)
				H-3 → L (17 %)
270/4.59	256/4.84	274/4.53 (S_{12})	0.0771	H → L+2 (54 %)
				H-10 → L (10 %)
		263/4.71 (S_{14})	0.1468	H-1 → L+1 (36 %)
				H-2 → L+1 (23 %)

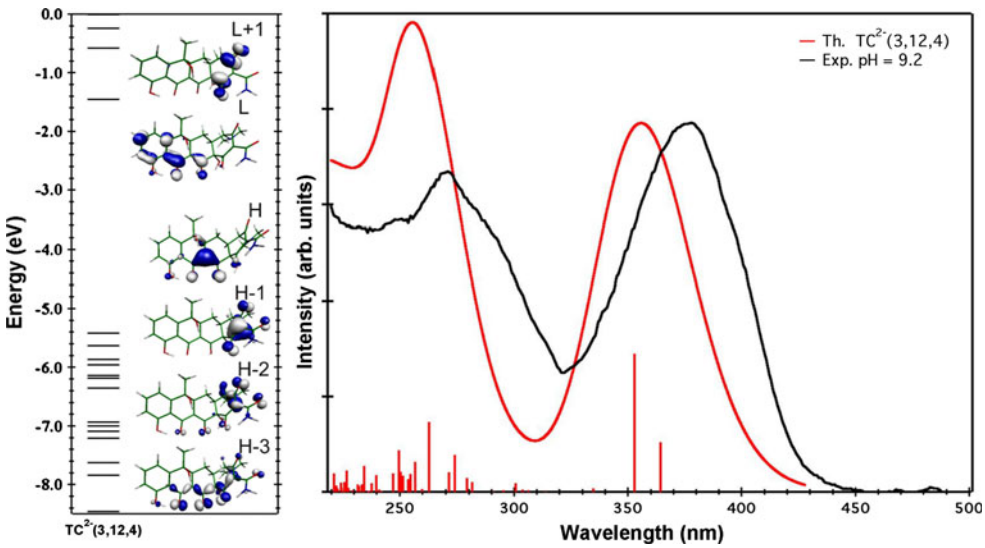

Fig. 5 *Left*: TC^{2-}(3,12,4) molecular orbital energies and isodensity plots. *Right*: Experimental spectrum pH = 9.2 (*black*) versus computed spectrum of TC^{2-}(3,12,4) (*red*)

5 Summary and conclusions

In this study, we have gained insight into the acid–base properties of tetracycline and its influence on the UV–vis spectra by means of DFT and TDDFT methodology. We calculated, for the first time, the pK_as of TCH_3^+ and of all the possible related deprotonated species, comparing calculated results to the experimental values. By computing the pK_a of each deprotonation step, we have been able to associate the species present at each pH, see Scheme 2. The absorption spectra of the most stable species arising from the stepwise deprotonation of TCH_3^+ have then been computed and compared to the experimental ones, allowing us to assign the transitions responsible for the absorption bands.

The calculated pK_as were in good agreement with experimental data, within ca. 1 pK_a unit, except for the third deprotonation for which the pK_a has been overestimated by more than 2 pK_a units. These latter data are probably due to an incomplete description of solvation effects, especially for the bi-anionic species for which explicit solvation could be relevant. The computed data indicate that the first deprotonation takes place in site 3 forming a zwitterionic species. The second deprotonation takes place in site 12 to form a mono-anionic species and the third one takes place in site 4 to form a di-anionic species.

The comparison of the computed spectra with the experimental ones shows that for the zwitterionic, the mono-anionic, and the di-anionic forms the first band is mainly due to π–π^* transitions involving the BCD chromophore. However, for the fully protonated TCH_3^+, the first band has a CT character from the BCD rings to the A ring.

We have demonstrated that DFT and TDDFT are accurate tools in defining a relationship between the deprotonation sites of tetracyclines and the experimental pK_as, and in computing their spectroscopic properties. The comparison between the computed pK_as and the experimentally determined values and between the simulated absorption spectra of specific deprotonated species and the measured spectra at given pHs points out the great contribution that computational chemistry can give to achieve a deeper comprehension in the acid–base chemistry of tetracycline compounds. The methodology described here can be therefore applied to other classes of compounds with relevant acid–base properties not completely accessible from the experiment.

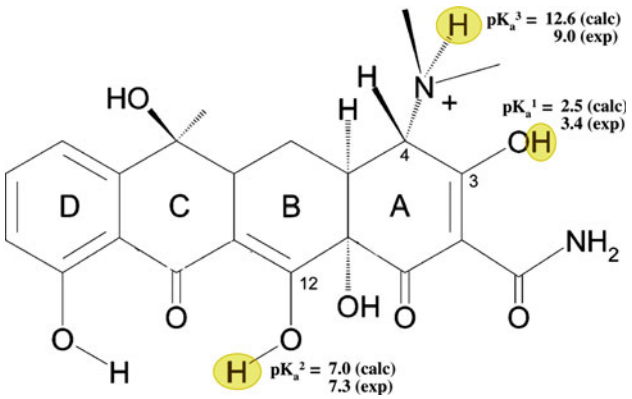

Scheme 2 Stepwise deprotonation of TCH_3^+. Computed and experimental pK_a

6 Supporting information available

Coordinates (xyz) of all the studied geometries optimized in solvent, scheme with the main distances and angles for the TC^+ conformations (twisted and extended), experimental absorption spectra at different pH, spectra of the main species computed using PBE0 and M06, comparison between the computed absorption spectrum of the TCH^-(3,4) species and the experimental one at pH = 8.5.

Acknowledgments AA, SF, and FDA thank Fondazione Istituto Italiano di Tecnologia, Project SEED 2009 "HELYOS", and MIUR-PRIN 2008 (2008CSNZFR) for financial support. BC and FE gratefully acknowledge the financial support of the Ministero per l'Università e la Ricerca Scientifica e Tecnologica (Rome, Italy) and the University of Perugia [PRIN 2008, n. 20088NTBKR] and the Fondazione Cassa di Risparmio di Perugia.

References

1. Carlotti B, Fuoco D, Elisei F (2010) Fast and ultrafast spectroscopic investigation of tetracycline derivatives in organic and aqueous media. Phys Chem Chem Phys 12:15580–15591
2. Othersen OG, Beierlein F, Lanig H, Clark T (2003) Conformations and Tautomers of Tetracycline. J Phys Chem B 107:13743–13749
3. Hillen W, Berens C (2002) Tetracyclin controlled gene regulation: from bacterial origin to eukaryotic tools. BIOspektrum 8:355–358
4. Hinrichs W, Kisker C, Düvel M, Müller A, Tovar K, Hillen W, Saenger W (1994) Structure of the Tet repressor-tetracycline complex and regulation of antibiotic resistance. Science 264:418–420
5. Hinrichs W, Fenske ChG (2001) In: Nelson M, Hillen W, Greenwald RA (eds) Tetracyclines in Biology, Chemistry and Medicine. Birkhäuser Verlag, Basel, pp 107–123
6. Gatz C, Quail PH (1998) Tn10-encoded tet repressor can regulate an operator-containing plant promoter. Proc Natl Acad Sci 85:1394–1397
7. Gossen M, Bujard H (2001) In: Nelson M, Hillen W, Greenwald RA (eds) Tetracyclines in Biology, Chemistry and Medicine. Birkhäuser Verlag, Basel, pp 139–157
8. Copra I, Roberts M (2001) Tetracycline Antibiotics: Mode of Action, Applications, Molecular Biology, and Epidemiology of Bacterial Resistance. Microbiol Mol Biol Rev 65:232–260

9. Nelson ML, Ismail MY (2007) The antibiotic and nonantibiotic tetracyclines. Elsevier, Amsterdam
10. Hanemaaijer R, van Lent N, Sorsa T, Salo T, Konttinen YT, Lindeman J (2001) In: Nelson M, Hillen W, Greenwald RA (eds) Tetracyclines in Biology, Chemistry and Medicine. Birkhäuser Verlag, Basel, pp 267–281
11. Schneider S, Schmitt MO, Brehm G, Reiher M, Matousek P, Towrie M (2003) Fluorescence kinetics of aqueous solutions of tetracycline and its complexes with Mg^{2+} and Ca^{2+}. Photochem Photobiol Sci 2:1107–1117
12. Carlotti B, Cesaretti A, Elisei F (2012) Complexes of tetracyclines with divalent metal cations investigated by stationary and femtosecond-pulsed techniques. Phys Chem Chem Phys 14:823–834
13. D'Agostino P, Ferlazzo V, Milano S, La Rosa M, Di Bella G, Caruso R, Barbera C, Grimaudo S, Tolomeo M, Feo S, Cillari E (2003) Chemically modified tetracyclines induce cytotoxic effects against J774 tumour cell line by activating the apoptotic pathway. Int Immunopharmacol 3:63–73
14. Hatsu M, Sasaki T, Gomi S, Kodama Y, Sezaki M, Inouye S, Kondo S (1992) A new tetracycline antibiotic with antitumor activity. I. Taxonomy and fermentation of the producing strain, isolation and characterization of SF2575. J Antibiot 45:320–324
15. Hatsu M, Sasaki T, Gomi S, Kodama Y, Sezaki M, Inouye S, Kondo S (1992) A new tetracycline antibiotic with antitumor activity. II. The structural elucidation of SF2575. J Antibiot 45: 325–330
16. Duivenvoorden WCM, Popovic SV, Lhotak S, Seidlitz E, Hirte HW, Tozer RG, Singh G (2002) Doxycycline Decreases Tumor Burden in a Bone Metastasis Model of Human Breast Cancer. Cancer Res 62:1588–1591
17. Lokeshwar BL, Selzer MG, Zhu BQ, Block NL, Golub LM (2002) Inhibition of cell proliferation, invasion, tumor growth and metastasis by an oral non-antimicrobial tetracycline analog (COL-3) in a metastatic prostate cancer model. Int J Cancer 98:297–309
18. Connell SR, Tracz DM, Nierhaus KH, Taylor DE (2003) Ribosomal protection proteins and their mechanism of tetracycline resistance. Antimicrob Agents Chemother 47:3675–3681
19. Nelson ML, Park BH, Levy SB (1994) Molecular Requirements for the Inhibition of the Tetracycline Antiport Protein and the Effect of Potent Inhibitors on the Growth of Tetracycline-Resistant Bacteria. J Med Chem 37:1355–1361
20. Bastos LFS, Merlo LA, Rocha LTS, Coelho MM (2007) Characterization of the antinociceptive and anti-inflammatory activities of doxycycline and minocycline in different experimental models. Eur J Pharmacol 576:171–179
21. D'Agostino P, Ferlazzo V, Milano S, La Rosa M, Di Bella G, Caruso R, Barbera C, Grimaudo CS, Tolomeo M, Feo S, Cillari E (2001) Anti-inflammatory effects of chemically modified tetracyclines by the inhibition of nitric oxide and interleukin-12 synthesis in J774 cell line. Int Immunopharmacol 1:1765–1776
22. Howlett DR, George AR, Owen DE, Ward RV, Markwell RE (1999) Common structural features determine the effectiveness of carvedilol, daunomycin and rolitetracycline as inhibitors of Alzheimer b-amyloid fibril formation. Biochem J 343:419–423
23. Cosentino U, Varí M, Saracino AG, Pitea D, Moro G, Salmona M (2005) Tetracycline and its analogues as inhibitors of amyloid fibrils: searching for a geometrical pharmacophore by theoretical investigation of their conformational behavior in aqueous solution. J Mol Model 11:17–25
24. Cosentino U, Pitea D, Moro G, Saracino AG, Caria P, Varì R, Colombo L, Forloni G, Tagliavini F, Salmona M (2008) The anti-fibrillogenic activity of tetracyclines on PrP 106-126: a 3D-QSAR study. J Mol Model 14:987–994
25. Ermak G, Cancasci VJ, Davies KJA (2003) Cytotoxic effect of doxycycline and its implications for tet-on gene expression systems. Anal Biochem 318:152–154
26. Frost P, Weinstein GD, Gomez EC (1971) Methacycline and Demeclocycline in Relation to Sunlight. J Am Med Assoc 216: 326–329
27. Frost P, Weinstein GD, Gomez EC (1972) Phototoxic Potential of Minocycline and Doxycycline. Arch Dermatol 105:681–683
28. Hasan T, Kochevar IE, McAuliffe DJ, Cooperman BS, Abdulah D (1984) Mechanism of Tetracycline Phototoxicity. J Invest Dermatol 83:179–183
29. Kulshrestha P, Sukmar N, Murray JS, Giese RF, Wood TD (2009) Computational Prediction of Antibody Binding Sites on Tetracycline Antibiotics: Electrostatic Potentials and Average Local Ionization Energies on Molecular Surfaces. J Phys Chem A 113:756–766
30. Dos Santos HF, Nascimento CS, Belletato P, De Almeida WB (2003) The conformational and tautomeric equilibrium of 5a,6-anhydrotetracycline in aqueous solution at pH 7. J MoL Struc (THEOCHEM) 626:305–319
31. Hussein W, Walker CG, Peralta-Inga Z, Murray JS (2001) Computed electrostatic potentials and average local ionization energies on the molecular surfaces of some tetracyclines. Int J Quant Chem 82:160–169
32. Murray JS, Peralta-Inga Z, Politzer P (2000) Computed molecular surface electrostatic potentials of the nonionic and zwitterionic forms of glycine, histidine, and tetracycline. Int J Quant Chem 80:1216–1223
33. Marcial BL, Costa LAS, De Almeida WB, Anconi CPA, Dos Santos HF (2011) Interaction of chemically modified tetracyclines with catalytic Zn(II) ion in matrix metalloproteinase: evidence for metal coordination sites. Theor Chem Acc 128:377–388
34. Marcial BL, Costa LAS, De Almeida WB, Dos Santos HF (2000) Structure and properties of the new complexes of platinum (II) with the chemically modified tetracycline CMT-3: A theoretical DFT study. J Mol Struc (THEOCHEM) 916:94–104
35. Othersen OG, Weibel R, Lanig H, Gmeiner P, Clark T (2006) SCRF-DFT and NMR Comparison of Tetracycline and 5a,6-Anhydrotetracycline in Solution. J Chem Phys B 110: 24766–24774
36. Meindl K, Clark T (2005) Conformations and Tautomers of 5a,6-Anhydrotetracycline. J Chem Phys B 109:4279–4284
37. Nicolas I, Vilchis M, Aragon M, Miranda R, Hojer G, Castro M (2003) Theoretical study of the structure and antimicrobial activity of horminone. Int J Quant Chem 93:411–421
38. Leypold CF, Reiher M, Brehm G, Schmidtt MO, Schneider S, Matousek P, Towrie M (2003) Tetracycline and derivatives—assignment of IR and Raman spectra via DFT calculations. Phys Chem Chem Phys 5:1149–1157
39. Marcial BL, Costa LAS, De Almeida WB, Dos Santos HF (2008) Reactivity of 5a,6-anhydrotetracycline platinum(II) complex with biological nucleophiles: a theoretical study. J Braz Chem Soc 19:1437–1449
40. Dos Santos HF, Marcial BL, De Miranda CF, Costa LAS, De Almeida WB (2006) Structure and properties of the 5a,6-anhydrotetracycline–platinum(II) dichloride complex: A theoretical ab initio study. J Inorg Biochem 100:1594–1605
41. De Almeida WB, Costa LAS, Dos Santos HF, Zerner MC (1997) A theoretical investigation of the near UV and VIS electronic spectra for the fully deprotonated forms of anhydrotetracycline. J Chem Soc, Perkin Trans 2:1335–1339
42. Duarte HA, Carvalho S, Paniago EB, Simas AM (1999) Importance of tautomers in the Chemical Behavior of Tetracyclines. J Phar Sci 88:111–120

43. Schmitt MO, Schneider S, Nelson ML (2007) Novel Insight into the Protonation/Deprotonation Equilibria of Tetracycline and Several Derivatives in Aqueous Solution. II. Analysis of the pH-Dependent Fluorescence Spectra by the SVD Technique. Z Phys Chem 221:235–271
44. Rigler NE, Bag SP, Leyden DE, Sudmeier JL, Reilley CN (1965) Determination of a protonation scheme of tetracycline using nuclear magnetic resonance. Anal Chem 37:872–875
45. Qiang Z, Adams C (2004) Potentiometric determination of acid dissociation constants (pK_a) for human and veterinary antibiotics. Water Res 38:2874–2890
46. Babic S, Horvat AJM, Mutavdzic Pavlovic D, Kastelan-Macan M (2007) Determination of pK_a values of active pharmaceutical ingredients. Trends Anal Chem 26:1043–1061
47. Dos Santos HF, De Almeida WB, Zerner MC (1998) Conformational analysis of the anhydrotetracycline molecule: a toxic decomposition product of tetracycline. J Pharm Sci 87:190–195
48. Amat A, Clementi C, De Angelis F, Sgamellotti A, Fantacci S (2009) Absorption and emission of the apigenin and luteolin flavonoids: a TDDFT investigation. J Phys Chem A 113:15118–15126
49. Amat A, Rosi F, Miliani C, Sgamelloti A, Fantacci S (2011) Theoretical and experimental investigation on the spectroscopic properties of indigo dye. J Mol Struct 993:43–51
50. Amat A, Clementi C, Miliani C, Romani A, Sgamellotti A, Fantacci S (2010) Complexation of apigenin and luteolin in weld lake: a DFT/TDDFT investigation. Phys Chem Chem Phys 12:6672–6684
51. Hohenberg P, Kohn W (1964) Inhomogeneous Electron Gas. Phys Rev 136:864–871
52. Stratmann RE, Scuseria GE, Frisch MJ (1998) An Efficient Implementation of Time Dependent Density Functional Theory for the Calculation of Excitation Energies of Large Molecules. J Chem Phys 109:8218–8224
53. Bauernschmitt R, Ahlrichs R (1996) Treatment of electronic excitations within the adiabatic approximation of time dependent density functional theory. Chem Phys Lett 256:454–464
54. Casida ME, Jamorski C, Casida KC, Salahub DR (1998) Molecular excitation energies to high-lying bound states from time-dependent density-functional response theory: Characterization and correction of the time-dependent local density approximation ionization threshold. J Chem Phys 108:4439–4449
55. Gaussian 09 Revision A1 Frisch MJ, Trucks GW, Schlegel HB, Scuseria GE, Robb MA, Cheeseman JR, Scalmani G, Barone V, Mennucci B, Petersson GA, Nakatsuji H, Caricato M, Li X, Hratchian HP, Izmaylov AF, Bloino J, Zheng G, Sonnenberg JL, Hada M, Ehara M, Toyota K, Fukuda R, Hasegawa J, Ishida M, Nakajima T, Honda Y, Kitao O, Nakai H, Vreven T, Montgomery Jr JA, Peralta JE, Ogliaro F, Bearpark M, Heyd JJ, Brothers E, Kudin KN, Staroverov VN, Kobayashi R, Normand J, Raghavachari K, Rendell A, Burant JC, Iyengar SS, Tomasi J, Cossi M, Rega N, Millam NJ, Klene M, Knox JE, Cross JB, Bakken V, Adamo C, Jaramillo J, Gomperts R, Stratmann RE, Yazyev O, Austin AJ, Cammi R, Pomelli C, Ochterski JW, Martin RL, Morokuma K, Zakrzewski VG, Voth GA, Salvador P, Dannenberg JJ, Dapprich S, Daniels AD, Farkas Ö, Foresman JB, Ortiz JV, Cioslowski J, Fox DJ (2009) Gaussian, Inc., Wallingford CT
56. Becke AD (1993) Density-functional thermochemistry. III. The role of exact exchange. J Chem Phys 98:5648–5652
57. Lee C, Yang W, Parr RG (1998) Development of the Colle-Salvetti conelation energy formula into a functional of the electron density. Phys Rev B 37:785–789
58. Miehlich B, Savin A, Stoll H, Preuss H (1989) Results obtained with the correlation energy density functionals of becke and Lee, Yang and Parr. Chem Phys Lett 157:200–206
59. Rassolov VA, Ratner MA, Pople JA, Redfern PC, Curtiss LA (2001) 6-31G* basis set for third-row atoms. J Comp Chem 22:976–984
60. Clark T, Chandrasekhar J, Spitznagel GW, Schleyer PvR (1983) Efficient diffuse function-augmented basis sets for anion calculations. III. The 3-21+G basis set for first-row elements, Li–F. J Comp Chem 4:294–301
61. Cossi M, Rega N, Scalmani G, Barone V (2003) Energies, structures, and electronic properties of molecules in solution with the C-PCM solvation model. J Comp Chem 24:669–681
62. Amat A, De Angelis F, Sgamellotti A, Fantacci S (2008) Acid–base chemistry of luteolin and its methyl-ether derivatives: A DFT and ab initio investigation. Chem Phys Lett 462:313–317
63. Alunni S, De Angelis F, Ottavi L, Papavasileiou M, Tarantelli F (2005) Evidence of a Borderline Region between E1cb and E2 Elimination Reaction Mechanisms: A Combined Experimental and Theoretical Study of Systems Activated by the Pyridine Ring. J Am Chem Soc 127:15151–15160
64. Liptak MD, Shields GC (2001) Experimentation with different thermodynamic cycles used for pK_a calculations on carboxylic acids using complete basis set and Gaussian-*n* models combined with CPCM continuum solvation methods. Int J Quant Chem 85:727–741
65. Saracino GAA, Improta R, Barone V (2003) Absolute pK_a determination for carboxylic acids using density functional theory and the polarizable continuum model. Chem Phys Lett 373:411–415
66. da Silva C, da Silva E, Nascimento M (1999) Ab Initio Calculations of Absolute pK_a Values in Aqueous Solution I. Carboxylic Acids. J Phys Chem A 103:11194–11199
67. da Silva C, da Silva E, Nascimento M (2000) Ab Initio Calculations of Absolute pK_a Values in Aqueous Solution II. Aliphatic Alcohols, Thiols, and Halogenated Carboxylic Acids. J Phys Chem A 104:2402–2409
68. Liptak MD, Gross KC, Seybold PG, Feldgus S, Shield GC (2002) Absolute pK_a Determinations for Substituted Phenols. J Am Chem Soc 124:6421–6427
69. Liptak MD, Shields GC (2001) Accurate pK_a Calculations for carboxylic acids using complete basis set and gaussian-*n* models combined with CPCM continuum solvation methods. J Am Chem Soc 123:7314–7319
70. McQuarrie DM (1970) Statistical mechanics. Harper and Row, New York
71. Kelly CP, Cramer CJ, Truhlar DG (2006) Aqueous solvation free energies of ions and ion–water clusters based on an accurate value for the absolute aqueous solvation free energy of the proton. J Phys Chem B 110:16066–16081
72. Zhan CG, Dixon DA (2001) Absolute Hydration Free Energy of the Proton from First-Principles Electronic Structure Calculations. J Phys Chem A 105:11534–11540
73. Zhan CG, Dixon DA (2002) First-Principles Determination of the Absolute Hydration Free Energy of the Hydroxide Ion. J Phys Chem A 106:9737–9744
74. Tissandier MD, Cowen KA, Yong Feng W, Gundlach E, Cohen MH, Earhart AD, Coe JV (1998) The proton's absolute aqueous enthalpy and Gibbs free energy of solvation from cluster-ion solvation data. J Phys Chem A 102:7787–7794
75. Kelly CP, Cramer CJ, Truhlar DG (2005) A Density Functional Theory continuum solvation model for calculating aqueous solvation free energies of neutrals, ions, and solute–water clusters. J Chem Theory Comput 1:1133–1152
76. Gao D, Svoronos P, Wong PK, Maddalena D, Hwang J, Walker H (2005) pK_a of acetate in water: a computational study. J Phys Chem A 109:10776–10785
77. Cao Z, Lin M, Zhang Q, Mo Y (2004) Studies of Solvation Free Energies of Methylammoniums and Irregular Basicity Ordering

of Methylamines in Aqueous Solution by a Combined Discrete-Continuum Model. J Phys Chem A 108:4277–4282
78. Lu H, Chen X, Zhan CG (2007) First-Principles Calculation of pK_a for Cocaine, Nicotine, Neurotransmitters, and Anilines in Aqueous Solution. J Phys Chem B 111:10599–10605
79. Król M, Wrona M, Page CS, Bates PA (2006) Macroscopic pK_a Calculations for Fluorescein and Its Derivatives. J Chem Theory Comput 2:1520–1529
80. Tozer DJ, Amos RD, Handy NC, Roos BO, Serrano-Andres L (1999) Does density functional theory contribute to the understanding of excited states of unsaturated organic compounds? Mol Phys 97:859–868
81. Dreuw A, Head-Gordon M (2004) Failure of Time-Dependent Density Functional Theory for long-range charge-transfer excited states: The zincbacteriochlorin–bacteriochlorin and bacteriochlorophyll − spheroidene complexes. J Am Chem Soc 126:4007–4016
82. Zhao Y, Truhlar DG (2008) The M06 suite of density functionals for main group thermochemistry, thermochemical kinetics, noncovalent interactions, excited states, and transition elements: two new functionals and systematic testing of four M06-class functionals and 12 other functionals. Theor Chem Acc 120:215–241
83. Perdew JP, Burke K, Ernzerhof M (1996) Generalized gradient approximation made simple. Phys Rev Lett 77:3865–3868
84. Adamo C, Barone V (1999) Toward reliable density functional methods without adjustable parameters: The PBE0 model. J Chem Phys 110(6158):6169
85. Zhan CG, Bentley J, Chipman DM (1998) Volume polarization in reaction field theory. J Chem Phys 108:177–192
86. Cossi M, Barone V, Cammi R, Tomasi J (1996) Ab initio study of solvated molecules: a new implementation of the polarizable continuum model. Chem Phys Lett 255:327–335
87. Mennucci B, Cammi R, Tomasi J (1998) Excited states and solvatochromic shifts within a nonequilibrium solvation approach: A new formulation of the integral equation formalism method at the self-consistent field, configuration interaction, and multiconfiguration self-consistent field level. J Chem Phys 109:2798–2807
88. Barone V, Cossi M (1998) Quantum calculation of molecular energies and energy gradients in solution by a conductor solvent model. J Phys Chem A 102:1995–2001